

High-throughput Computational Study of Halide Double Perovskite Inorganic Compounds

Yao Cai,^{*,†} Wei Xie,[†] Yin Ting Teng,[‡] P. C. Harikesh,^{‡,§} Biplab Ghosh,^{‡,§} Patrick Huck,^{||} Kristin A. Persson,^{†,||} Nripan Mathews,^{‡,§} Subodh G. Mhaisalkar,^{‡,§} Matthew Sherburne,[†] and Mark Asta^{*,†,⊥}

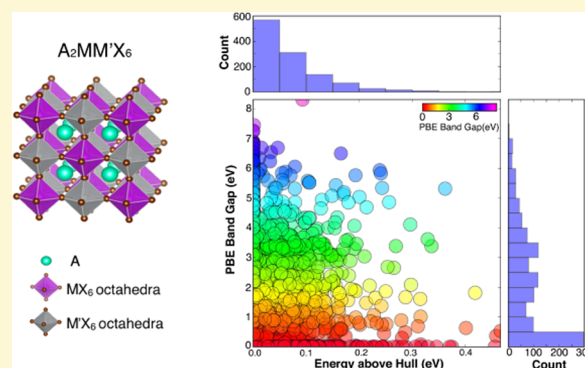
[†]Department of Materials Science and Engineering, University of California, Berkeley, California 94720, United States

[‡]Energy Research Institute@NTU (ERI@N), Interdisciplinary Graduate School and [§]School of Materials Science and Engineering, Nanyang Technological University, 637553 Singapore

^{||}Energy Storage and Distributed Resources Division and [⊥]Materials Sciences Division, Lawrence Berkeley National Laboratory, Berkeley, California 94720, United States

Supporting Information

ABSTRACT: Double perovskite halides are a class of materials with diverse chemistries that are amenable to solution-based synthesis routes, and display a range of properties for a variety of potential applications. Starting from a consideration of the octahedral and tolerance factors of ~ 2000 candidate double perovskite compounds, we compute structural, electronic, and transport properties of ~ 1000 using first-principles calculations based on density-functional-theory methods. The computational results have been assembled in a database that is accessible through the Materials Project online. As one potential application, double perovskites are candidates in the search for lead-free halide photovoltaic absorbers. We present the application of our database to aid the discovery of new double perovskite halide photovoltaic materials, by combining the results with optical absorption and phonon stability calculations. From three distinct classes of chemistries, 11 compounds were identified as promising solar absorbers and the complex chemical trends for band gap within each of these are analyzed, to provide guidelines for the use of substitutional alloying as a means of further tuning the electronic structure. Other possible applications of the database are also discussed.



INTRODUCTION

Double perovskite halides ($A_2MM'X_6$) are a class of compounds that can span diverse chemistries. The crystal structure (Figure 1a) is formed by corner-sharing octahedra with M or M' atoms at the centers and X atoms at corners. M and M' centers are ordered as second neighbors over the simple cubic cation sublattice and A atoms are in the center of eight neighboring octahedra. Due to their diverse chemistries, the family of halide double perovskites displays a range of electronic properties, making them candidates for a variety of applications, including photoabsorbers for solar cells, ultraviolet (UV) photodetectors, X-ray detector, and scintillators, etc. For example, thin-film $Cs_2AgBiBr_6$ photovoltaic (PV) devices have been demonstrated with power conversion efficiency (PCE) close to 2.5% and an open-circuit voltage exceeding 1 V;¹ additionally, sensitive and fast UV photodetectors based on $Cs_2AgInCl_6$ single crystals² and low detection limit X-ray detectors based on $Cs_2AgBiBr_6$ single crystal have been demonstrated,³ respectively; further, use of Cs_2LiYCl_6 has been demonstrated for the detection of γ rays, thermal, and fast neutrons simultaneously.⁴ The wide interest

and variety of potential applications of these compounds have motivated the current work, in which we have employed high-throughput computing using density-functional-theory (DFT)-based approaches to develop an open and searchable double perovskite halide database, which has been incorporated into the Materials Project database.⁵

One of the applications of double perovskite halides that has received significant attention recently is as absorber materials for solar cells.⁶ Many experimental and computational investigations related to such applications have been published since 2016. Single crystals of $Cs_2AgBiBr_6$ (indirect band gap 1.95 eV) were synthesized and shown to have a long room-temperature fundamental photoluminescence lifetime of 660 ns, high defect tolerance, and better heat and moisture stability compared with (MA)PbI₃.⁷ Another work demonstrated a long electron-hole diffusion length (>100 nm) in $Cs_2AgBiBr_6$ solar-cell devices with over 1% PCE.⁸ The hybrid double perovskite

Received: January 10, 2019

Revised: July 12, 2019

Published: July 12, 2019

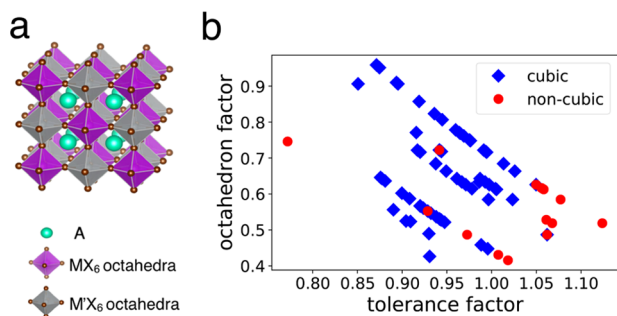


Figure 1. (a) Crystal structure of the cubic double perovskite compound with composition $A_2MM'X_6$. (b) A structure map for known halide $A_2MM'X_6$ compounds. Crystal structures reported in the ICSD are indicated by the different symbols, with blue diamonds and red circles corresponding to cubic and noncubic materials, respectively. For each material, the octahedral factor is calculated as $\frac{R_M + R_{M'}}{2R_X}$ and the tolerance factor is calculated as $\frac{R_A + R_X}{\sqrt{2}((R_M + R_{M'}) / 2 + R_X)}$, with R_A , R_M , $R_{M'}$, R_X representing the radii of the A, M, and M' site cations and the X-site halide anion, respectively. Shannon effective ionic radii for 12-coordinated A^{1+} cations, 6-coordinated M^{1+} and M'^{3+} cations, and 6-coordinated X^{1-} anions⁴⁵ are used for R_A , R_M , $R_{M'}$, and R_X .

$(MA)_2AgBiBr_6$ with a band gap of 2.02 eV was also synthesized.⁹ $Cs_2AgBiCl_6$ was synthesized and measured to possess an indirect band gap of 2.2–2.77 eV,¹¹ and Cs_2AgBiI_6 with a smaller 1.75 eV band gap was synthesized as nanocrystals via anion exchange.¹² A similar compound $Cs_2AgSbCl_6$ with an indirect band gap (2.54 eV)¹³ was also synthesized. Another double perovskite $(MA)_2KBiCl_6$ was synthesized and found to have a large indirect band gap of 3.04 eV.¹⁴ Indirect band gaps are not ideal for photovoltaic applications, and direct band gap materials are desired.¹⁵ Single-crystal $(MA)_2TlBiBr_6$ was synthesized and found to have a direct band gap of 2.0 eV.¹⁶ $Cs_2AgInCl_6$, a direct band gap compound with parity-forbidden band gap of 2.1 eV and absorption onset of 3.2 eV,² was shown to be photosensitive to UV light¹⁷ and to possess good moisture, light, and heat stability.¹⁸

As a means for further optimizing the properties of double perovskites for device applications, substitutional alloying or doping is expected to be a useful strategy. Band engineering with impurities in this system can dramatically alter the band edge structure. Dilute alloying of Tl into both Ag and Bi sites of $Cs_2AgBiBr_6$ decreases its band gap by 0.5 eV, with long-lived carriers with microsecond lifetimes.¹⁹ In (75%) and Sb (37.5%) can be alloyed into the host $Cs_2AgBiBr_6$ with In–Bi alloying increasing the band gap and Sb–Bi alloying decreasing the band gap to 1.86 eV at most.²⁰ Solid solutions between $Cs_2AgSbCl_6$ and $Cs_2AgInCl_6$ can be tuned to have either direct (below 40% Sb) or indirect (above 40% Sb) band gaps.¹³ A DFT study indicates that $Cs_2BiAg_{1-x}Cu_xCl_6$ mixtures should be amenable to synthesis with the band gap between 1.6 and 1.9 eV.²¹ Another DFT study indicates that mixed-cation (Cs/MA/FA)₂InBiBr₆ halide double perovskites have optoelectronic properties comparable to MAPbI₃.²²

Several previous investigations have focused on the use of computational methods to screen double perovskites for photovoltaic applications. Two double perovskites $Cs_2InSbCl_6$ and $Cs_2InBiCl_6$ isoelectronic to Pb halides (ns^2np^0) were proposed as promising candidates due to their good theoretical maximum solar-cell efficiencies.^{23,24} Also proposed were three

other double perovskites, $Cs_2AgInBr_6$, $Rb_2AgInBr_6$, and $Rb_2CuInCl_6$, that have direct band gaps with close to optimal values for solar absorbers.^{25,26} $Rb_2AgInCl_6$ and $Cs_2AgInCl_6$ with larger direct band gaps were also identified computationally.²⁷ A mixed-valence $Cs_2Au_2I_6$ (i.e., $Cs_2Au^{1+}Au^{3+}I_6$) compound was synthesized^{28,29} and was measured to have an optical gap of 1.31 eV.³⁰ In another high-pressure study, it was shown to have a band gap near 0.6 eV at 1.5 GPa.³¹ In a first-principles computational study, this compound was shown to be a direct gap semiconductor with a 1.21 eV band gap.³²

The experimental and computational research reviewed above has focused on ~50 halide double perovskite compositions, which is a relatively small subset of a large number of possible compositions. Consequently, an expanded computational screening effort that considers a wider range of chemical combinations is worthwhile. In this work, we have performed DFT-based high-throughput calculations considering ~1000 halide double perovskites. Based on our calculations, we have developed a double perovskite database, including all calculated structural information, energetics, and band gaps. The database covers chemistries identified starting with ~2000 candidate double perovskite compositions, considering empirical structural factors. These structural stability considerations lead to a down select to ~1000 compositions for which we employed semilocal DFT functionals to perform electronic structure calculations to obtain thermodynamic stability and a rough estimate of band gaps.

As an example of the use of this database, we present an application in screening for possible new photovoltaic (PV) materials and explore trends underlying the variation of the electronic structure with chemical composition. Double perovskites (30) from five categories are identified as possible candidates as solar absorbers. For these compounds, we employ hybrid functional methods with spin–orbit coupling to calculate and analyze the electronic structures in more detail. Important parameters for PV applications, such as band gaps, effective masses, absorption spectra, conversion efficiency, and phonon stability, are calculated. Compounds (11) from three classes of chemistries that are anticipated to be thermodynamically and structurally stable and have theoretical conversion efficiencies larger than 10% are identified. Several compounds from two of the three classes have been reported in previous experimental or computational studies (A_2AgInX_6 ,^{2,17,18,27} A_2CuInX_6 ,²⁵ A_2TlBiX_6 ,¹⁶ A_2InBiX_6 ,²³ and A_2InSbX_6 ,^{23,23} etc.), and our screening results are consistent with these reports. Furthermore, we propose one new category of compounds in this work: $A_2MM'X_6$ with $M = In, Tl$, $M' = Al, Ga, In, Tl$. For each of the three classes, chemical trends of band gaps are discussed, to provide guidance for the design of solid solutions that may enable further tuning of properties.

■ DATABASE DETAILS

In this section, we describe the methods underlying the development of the double perovskite computational database, the results of screening based on the consideration of tolerance and octahedral factors to identify the chemistries considered and an overview of the database information. The database of calculated values can be accessed through the Materials Project website (DOI: 10.17188/1476059, link: <https://materialsproject.org/materials/10.17188/1476059>).

Computational Methods. Calculations were carried out employing HSE06- and Perdew–Burke–Ernzerhof (PBE)-generalized gradient approximation (GGA)-based DFT

methods using the projector augmented wave (PAW) method,³³ as implemented in the Vienna Ab initio simulation package (VASP).^{34–36} The workflow used in this study was developed to consider the possibility of extending to broader ranges of chemistries, including those where spin-polarized ground states might be expected; as a consequence, all calculations were performed spin-polarized even though all of the resulting ground states were nonmagnetic. The PAW potentials used in the calculations are the same as those employed in the calculations underlying the data in Materials Project,⁵ to facilitate comparisons with the results available through this database. The self-consistency iterations were performed until the energy was converged to within 1×10^{-5} eV. Structural relaxations with respect to cell volume and ionic coordinates (ISIF = 3 in VASP) were undertaken until the forces were converged within 0.01 eV/Å for the GGA-PBE calculations and within 0.05 eV/Å for hybrid functional calculations. The symmetry for the space group $Fm\bar{3}m$ was kept throughout the relaxations. For some compounds, the ground state may be structurally distorted with a lower symmetry;^{29,37,38} in applications of the database, promising structures can be further examined for such structural distortions, as demonstrated below. The energy cutoff for the plane-wave basis for all compounds was set to 520 eV. Relaxation calculations were carried out with a γ -centered k -point mesh of $5 \times 5 \times 5$. Based on our convergence tests, this choice of plane-wave cutoff and k -point density is found to be sufficient to provide total energies converged to within 1 meV/atom and lattice constants within 0.01 Å.

To obtain more accurate electronic structures for selected compounds, band structures and density of states were calculated by PBE with spin-orbit coupling (SOC) corrections, with conduction bands corrected to match the HSE06 + SOC band gaps employing a simple “scissor operator”. Spin-orbit coupling was included using the approach available in VASP. For density of states calculations, a γ -centered k -point mesh of $10 \times 10 \times 10$ and the tetrahedron method with Blöchl corrections³⁹ were used for k -space integration. For band structure calculations, k -points were sampled along high-symmetry lines in the Brillouin zone.

The energy above hull (i.e., the difference in energy between a given compound and the compound or phase-separated combinations of compounds that have the lowest energy at the associated composition) was calculated by retrieving the total energies of all available compounds in the A–M–M′–X system from Materials Project, including common allotropes, binary, and ternary compounds. The average effective masses⁴⁰ were calculated using the BoltzTrap code⁴¹ and the pymatgen package.^{40,42} γ -centered $20 \times 20 \times 20$ k -point meshes were used for GGA-PBE band structure calculations. The band structures were then used as the input to the BoltzTrap code to calculate the conductivity tensor $\frac{\sigma(T, \mu)}{\tau}$, with τ the constant relaxation time, T the absolute temperature (set to 300 K), and μ the Fermi level. Then, averaged effective masses were calculated as $\mathbf{m} = \frac{ne^2\tau}{\sigma}$. As mentioned by Hautier et al.,⁴⁰ the effective mass defined in this way is an average of $\mathbf{m}(i, \mathbf{k})$ around the Fermi level μ , with i the index of the band and \mathbf{k} the wave vector. For electron effective mass, μ was set at the conduction band minimum (CBM); for hole effective mass, μ was set at the valence band maximum (VBM). The convergence of the effective mass values with respect to the

density of k -points, over which the band structure was sampled, was carefully tested, and the values were found to be converged to within 1% using a $20 \times 20 \times 20$ mesh.

Absorption spectra were calculated from the frequency-dependent dielectric function within the independent-particle picture with PBE functionals and corrected by the scissor operator to match the HSE band gap values. The number of bands used in the calculations are 4 times the number of occupied bands. γ -centered $10 \times 10 \times 10$ k -point meshes were used in the calculation. The spectroscopic limited maximum efficiency (SLME) was calculated based on the absorption spectra, following an approach due to Yu and Zunger.⁴³

To investigate the structural stability, phonon spectra were calculated using the finite displacement method employing VASP with the Phonopy package.⁴⁴ The primitive structures were first relaxed with a higher force-tolerance criterion of 10^{-4} eV/Å. A $2 \times 2 \times 2$ supercell and a $4 \times 4 \times 4$ k -point mesh were used for the finite displacement calculations.

Chemistries Considered. In this section, we provide a brief description of the chemical compositions of the $A_2MM'X_6$ inorganic compounds considered in the present computational study. We start by considering 1980 double perovskite compounds of the elpasolite type (Figure 1a) with alkali atoms $A = \text{Li, Na, K, Rb, Cs}$, monovalent cations $M = \text{Li, Na, K, Rb, Cs, Cu, Ag, Au, Hg, In, Tl}$, trivalent cations $M' = \text{Sc, Y, Al, Ga, In, Tl, As, Sb, Bi}$, and the halide anions $X = \text{F, Cl, Br, I}$. To further motivate the choice of structure and chemistries considered in the calculations, we show in Figure 1b a structure map similar to those used in studies of perovskite-based compounds.⁴⁶ The axes in this figure correspond to the octahedral factor and the Goldschmidt’s tolerance factor.

The octahedral factor is defined as the ratio between average (M, M') cation Shannon radii for 6-fold coordination and X anion Shannon radii for 6-fold coordination.⁴⁵ The tolerance factor is calculated by replacing the M radius in the standard expression for the perovskite tolerance factor⁴⁷ with the average radius of (M, M'). For perovskite compounds, the octahedral factor is used empirically to predict the formation of the MX_6 octahedron; and the tolerance factor is used empirically to predict the formation and distortion of the perovskite structure. Likewise, in the $A_2MM'X_6$ double perovskite structure, we can combine the octahedral factor and tolerance factor to predict the formation and distortion of the structure.

Small octahedral factors suggest that the formation of MX_6 octahedra is disfavored. According to the survey of known $A_2MM'X_6$ compounds in the ICSD database,^{48,49} shown in Figure 1b, most known compounds are face-centered cubic ($Fm\bar{3}m$) and are indicated by blue diamonds. Thus, this work focuses on the consideration of such cubic structures with a $Fm\bar{3}m$ space group. On the other hand, as shown in Figure 1b, compounds with larger tolerance factor and smaller octahedral factor tend to form noncubic structures, as indicated by red circle symbols. The crystallographic details of the experimentally observed double perovskite structures are listed in Table S1. The limits of the octahedral factor and tolerance factor for cubic structures indicated by the above survey are used empirically as the first screening criteria to reduce the 1980 compounds by approximately half, to a number of 1149 compounds selected for further consideration by DFT-based methods. The limits set for tolerance factor is (0.82, 1.08) and for octahedral factor (0.4, 1.0). More discussions on tolerance factor and octahedral factor can be found in the Supporting

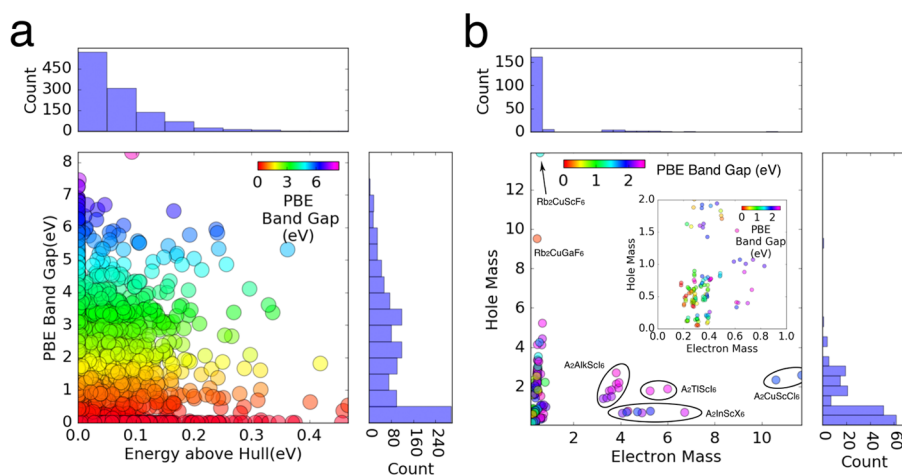


Figure 2. (a) Distribution of calculated energy above the hull and PBE band gap. The scatter plot illustrates the distribution of calculated energies above hull and band gap values for 1149 cubic double perovskite halide compounds. The histograms quantify the distribution of the calculated values for the compounds considered. (b) The distribution of calculated effective mass and PBE band gap values. The scatter plot illustrates the distribution of electron mass and hole mass for 189 double perovskite halides with $E_{\text{hull}} < 50$ meV/atom and $0.1 \text{ eV} < E_g < 2.5 \text{ eV}$. The histograms quantify the distribution of the calculated values for the compounds considered. Inset: zoom-in view showing only materials with small effective masses.

Information, where we also consider the implications of the use of a modified set of ionic radii due to Travis et al.⁵⁰

Overview of Database. In Figure 2a, we present the distribution of the calculated energy above hull and PBE band gap of all double perovskite halides that are within the determined limits for tolerance factor and octahedral factor identified in the previous section. In a survey by Sun et al.,⁵¹ for experimentally observed fluorides, chlorides, bromides, and iodides, the energies above hull are under 100, 50, 30, 25 meV/atom, respectively. In the current study, we used these thresholds to screen for stable or metastable compounds. It should be pointed out that the Materials Project database does not contain all possible decomposition products for some of the compounds, so that the calculated energy above hull serves only as a lower bound such that the actual thermodynamic (meta)stability could be lower than predicted. It should also be pointed out that these are zero-temperature calculations, and the stability could be altered by finite temperature contributions to the free energy. In other words, some of the compounds that are predicted to be unstable at 0 K might turn out to be stable at room temperature due to the entropy terms in free energy. The consideration of finite temperature stabilities can be undertaken as further efforts in applications of the database studied here, which are limited to zero-temperature properties. Related to finite temperature effects, practical applications of halide perovskites are often limited by their stability in air and moisture, and the examination of such effects computationally would again require additional efforts to compute reaction energetics that outside the scope of the database presented here.

Employing the bounds on energy above hull (i.e., considering only fluorides, chlorides, bromides, and iodides with energy above hull lower than 100, 50, 30, 25 meV/atom, respectively) narrows down the search space for synthesizable double perovskite halides to 238 fluorides, 161 chlorides, 107 bromides, and 37 iodides (543 in total). The calculated PBE band gaps of these 543 compounds span from 0 to 8 eV, which indicates a rich variety of electronic properties, covering metals, semiconductors, and large-gap insulators. Out of the 543 compounds, 62, 171, and 310 have PBE-calculated band

gaps (E_g) of 0, $0 < E_g < 2.5$, $E_g \geq 2.5$, respectively. From the scatter plot in Figure 2a, we can observe that compounds with the highest values of the energy above hull (i.e., more unstable) are more likely to be those predicted as metals.

To evaluate the transport properties of these compounds, we have calculated effective masses. In Figure 2b, we presented the distribution of effective masses and PBE band gaps of 189 double perovskite halides with the energy above hull (E_{hull}) having values < 50 meV/atom and $0.1 \text{ eV} < E_g < 2.5 \text{ eV}$. Interestingly, most of the compounds have very small electron effective masses (167 compounds with $m_e < 1$), but overall a relatively broad distribution of hole effective masses. The groups of outliers are indicated in the scatter plot, and most of them have Sc as the M' cation. It is interesting that Sc compounds have such a broad range of effective mass values. For example, $\text{Rb}_2\text{CuScF}_6$ has a very small electron mass and a very large hole mass, whereas $\text{Rb}_2\text{CuScCl}_6$ has a very large electron mass and an intermediate value of hole mass. The hybridization in Sc–Cl and Cu–Cl states is relatively stronger than for Sc–F and Cu–F, so Cu-d band (valence band) and Sc-d band (conduction band) are narrower in $\text{Rb}_2\text{CuScF}_6$ than in $\text{Rb}_2\text{CuScCl}_6$, thus the effective mass should be larger in $\text{Rb}_2\text{CuScF}_6$, which is true for the hole mass. However, it happens that in $\text{Rb}_2\text{CuScF}_6$, at the conduction band edge, there is also some hybridization from Cu-s and F-s, which contributes to a very small electron mass. In $\text{Rb}_2\text{CuScCl}_6$, the Cu-s and Cl-s also hybridize, but the energy level is higher than the conduction edge and thus has no contribution to electron effective mass. Other Sc compound outliers in Figure 2b generally have large electron mass due to the narrow Sc-d band that dominates the character of the conduction band edge. Notably, $M/M' = \text{In}/\text{Sc}$ compounds have small hole masses due to strong In-s/X-p hybridization at the valence band and might be good for hole transport materials. In the current study, we are particularly interested in materials with low electron and hole masses, so in the inset of Figure 2b, we show only the compounds with small effective masses. There is a rough trend that compounds with larger band gap (represented by purple/blue dots) have larger effective masses than

compounds with smaller band gap (represented by red/yellow/green dots).

■ ANALYSIS FOR SOLAR ABSORBER APPLICATIONS

Promising Candidates from the Database. Among double perovskite halide compounds that satisfy the energy above hull criteria defined in the previous section, only 30 compounds satisfy the following conditions: PBE band gaps with $E_g > 0$ (nonmetal), $E_{g(\text{direct})} < 1.5$ eV, and effective masses with $0 < m_e, m_h < 1.5$. Such compounds are considered as potentially interesting candidates for photovoltaic applications and are the focus of further analysis. Specifically, for these 30 compounds, we further relax the structure using the HSE functional and calculate band gaps using the HSE functional with SOC included.

We consider first a comparison of the calculated and measured lattice constant of $\text{Cs}_2\text{AgBiBr}_6$, $\text{Cs}_2\text{AgBiCl}_6$, and $\text{Cs}_2\text{AgInCl}_6$. Note that $\text{Cs}_2\text{AgBiBr}_6$ and $\text{Cs}_2\text{AgBiCl}_6$ are experimentally observed but do not belong to the predicted 30 promising candidates. The calculated and measured lattice constants agree reasonably well with the GGA-PBE value (11.49, 10.96, and 10.68 Å), which are larger than measurements (11.25,⁷ 10.78,¹⁰ and 10.47 Å¹⁷) by up to 2.1%. The calculated results from HSE06 (10.60 Å for $\text{Cs}_2\text{AgInCl}_6$) show slightly better agreement with measurements, with a deviation of up to 1.3%. Supporting Information Table S2 lists calculated results for the lattice constants of the 30 $\text{A}_2\text{MM}'\text{X}_6$ compounds that passed the screening criteria described above and also compares and shows that the present GGA-PBE-calculated lattice constants are consistent with previous calculations using the same method.

Band gaps, energies above hull and effective masses of the 30 compounds are listed in the Supporting Information Tables S3 and S4, respectively. For these 30 compounds, except for $\text{Cs}_2\text{AgInCl}_6$, all other compounds have not been experimentally realized as reported in the Inorganic Crystal Structure Database.^{48,49} Among the 30 compounds, 12 compounds are predicted to be thermodynamically stable ($E_{\text{hull}} = 0$), including $\text{Cs}_2\text{AgInCl}_6$. The HSE06 + SOC-calculated band gaps span the range of 0.2–2.6 eV. We also list in Table S3 some of the measured band gaps and calculated HSE06 + SOC band gaps from the other work. The present calculated HSE06 + SOC band gap for $\text{Cs}_2\text{AgInCl}_6$ (2.57 eV) is very close to a previous HSE06 calculation (2.6 eV)¹⁷ without SOC, indicating that SOC effects are not significant for In/Ag double perovskites. Both calculations give band gap values somewhat smaller than measurements (3.3 eV).¹⁷ We further compare our HSE + SOC calculations with previous calculations for additional compounds in Table S3; results are largely consistent with the small differences likely due to the fact that the calculated band gaps are sensitive to the lattice constant and our calculations are based on HSE06-relaxed structures, whereas previous calculations are based on PBE-relaxed structures.²³

The 30 compounds are divided into five categories according to their M and M' site elements. The five categories are listed in Table 1. For category 1 and category 2 compounds, M and M' cations have the same electron configurations (both $d^{10}s^0$ or both $d^{10}s^2$), which leads to a direct band gap. For all other categories, M and M' cations have mismatched electron configurations, which leads to an indirect band gap. Category 3 and category 5 actually have the same mismatched electron configurations ($d^{10}s^2/d^{10}s^0$), and it is expected that they have similar electronic structures.

Table 1. Five Categories of Promising Candidates^a

category	M	M'	electron configuration	band gap
1	Cu, Ag, Au	Al, Ga, In, Tl	$d^{10}s^0/d^{10}s^0$	direct
2	In, Tl	As, Sb, Bi	$d^{10}s^2/d^{10}s^2$	direct
3	Cu, Ag, Au	As, Sb, Bi	$d^{10}s^0/d^{10}s^2$	indirect
4	Cu, Ag, Au	Sc, Y	$d^{10}s^0/p^6$	indirect
5	In, Tl	Al, Ga, In, Tl	$d^{10}s^2/d^{10}s^0$	indirect

^aElectron configurations and band gap types are listed.

Similar to halide perovskite AMX_3 ⁵² and derivative A_2MX_6 ⁵³ compounds, in the chemical series K, Rb, and Cs, the band gap slightly increases (for example, $\text{K}_2\text{AgInCl}_6$ (2.49 eV) to $\text{Rb}_2\text{AgInCl}_6$ (2.52 eV) to $\text{Cs}_2\text{AgInCl}_6$ (2.57 eV)); from Cl to Br to I, the band gap decreases more strongly (for example, $\text{Rb}_2\text{AgInCl}_6$ (2.52 eV) to $\text{Rb}_2\text{AgInBr}_6$ (1.44 eV) and $\text{Rb}_2\text{TlSbBr}_6$ (1.03 eV) to $\text{Rb}_2\text{TlSbI}_6$ (0.57 eV)). The chemical trends for M and M' site elements are more complex and will be discussed further below.

We consider next the results for effective masses listed in the Supporting Information Table S4. Our calculated average effective masses are consistent with previous calculations, even though previous calculations are based on PBE + SOC band structures and our calculations are based on PBE band structures. The chemical trends in effective mass values listed in Table S4 are correlated with those for the band gaps. Specifically, increasing the size of the A-site cation leads to an increase in both the effective mass and the band gap; increasing the size of the X-site anion leads to a decrease in both the effective mass and the band gap. This correlation between band gap and effective mass is consistent with the k - p theory.⁵⁴ If we only consider the effective mass, among the five categories, the In/Tl–As/Bi/Sb compounds are the best candidates for high mobilities, desirable for photovoltaic applications, since they have small effective mass for both electrons and holes.

Band Structure. In Figure 3, we present calculated band structures and densities of states (DOS) for one representative compound from each of categories listed in Table 1. Since categories 3 and 5 have the same electron configurations, only the representative compound from category 5 is shown.

We consider first the electronic structure of $\text{Cs}_2\text{AgInBr}_6$ (Figure 3a), representative of the set of compounds with M = Cu, Ag, Au and M' = Al, Ga, In, Tl (from category 1). It is calculated to be a direct band gap semiconductor with valence band derived from antibonding states of Ag-d and Br-p orbitals and conduction band derived from antibonding states of In-s and Br-p orbitals. The direct nature of the band gap of $\text{Cs}_2\text{AgInBr}_6$ is consistent with previous ab initio calculations.²⁵ The conduction band is very dispersive (s character), leading to its small electron effective mass ($0.18m_e$). The valence band edge consists of a heavy hole band and a light hole band, and the average hole effective mass ($0.71m_e$) is, thus, larger than the electron effective mass.

We consider next the representative compound $\text{Cs}_2\text{InBiCl}_6$ for the set of compounds with M = In, Tl and M' = As, Sb, Bi (from category 2). The calculated band structure in Figure 3b shows that this compound is a direct band gap semiconductor with valence band derived primarily from antibonding states between In-s and Cl-p orbitals and conduction band primarily from antibonding states between Bi-p and Cl-p orbitals. The direct nature of the band gap of $\text{Cs}_2\text{InBiCl}_6$ is consistent with

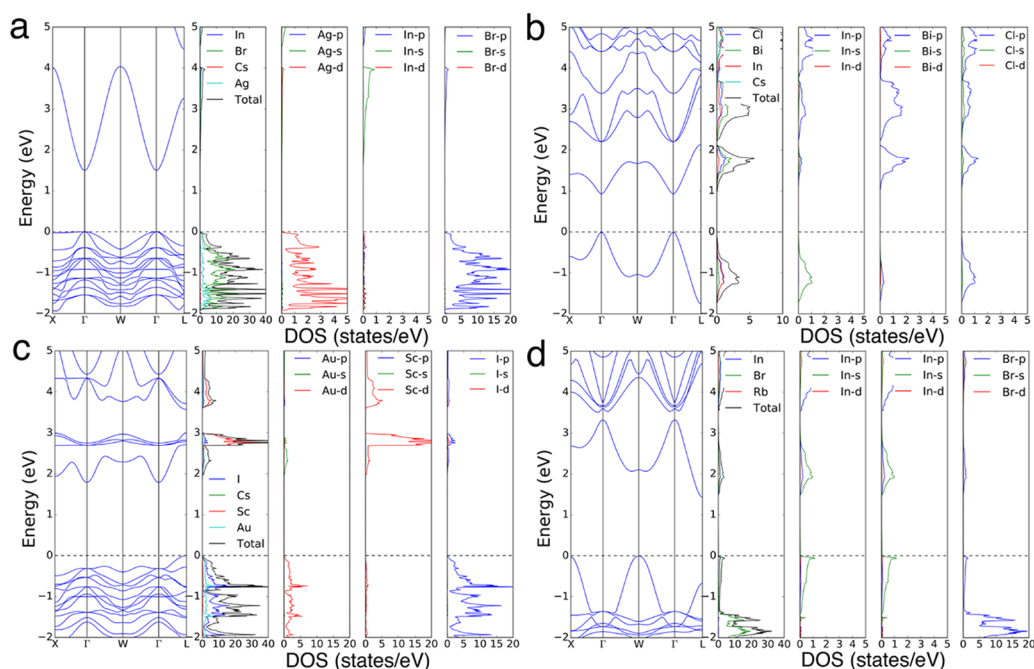


Figure 3. Band structures, total and projected densities of states (DOS), calculated by PBE + SOC with conduction bands shifted to match calculated HSE06 + SOC band gaps by a scissor operator for (a) $\text{Cs}_2\text{AgInBr}_6$ (category 1), (b) $\text{Cs}_2\text{InBiCl}_6$ (category 2), (c) $\text{Cs}_2\text{AuScI}_6$ (category 4), and (d) $\text{Rb}_2\text{InInBr}_6$ (category 5).

previous ab initio calculations.²³ The dispersive nature of both the conduction band and valence band leads to the small electron and hole effective mass ($0.39m_e$ and $0.18m_e$). The dispersive valence band derives from the *s* orbitals of the cations.

Next, we consider the compound $\text{Cs}_2\text{AuScI}_6$ representative of the set of compounds with $M = \text{Cu, Ag, Au}$ and $M' = \text{Sc, Y}$ (from category 4). The calculated band structure in Figure 3c shows that it is an indirect gap semiconductor with the valence band derived primarily from antibonding states between Au-d and I-p orbitals and the conduction band derived from both antibonding states between Au-s and I-p orbitals and antibonding states between Sc-d and I-p orbitals. To the best of our knowledge, no experimental results have been reported for any of the compounds in this category. The conduction band is more dispersive than the valence band, resulting in a smaller electron effective mass ($0.23m_e$) than hole effective mass ($0.64m_e$).

We consider finally $\text{Rb}_2\text{InInBr}_6$, representative of the set of compounds with M and M' from the same group (Al, Ga, In, Tl) in the periodic table (from category 5). The calculated band structure in Figure 3d shows that it is an indirect band gap semiconductor with different cation configurations ($\text{In-d}^{10}s^0$, $\text{In-d}^{10}s^2$). If the two In ions in the primitive unit cell are in the same charge state, with one unpaired *s* electron, we would expect RbInBr_3 to be a metallic conductor. Indeed, forcing a single charge state for In by using a 5-atom unit cell results in a metallic state. Charge ordering between different valence states on the In site leads to the semiconductor state in Figure 3d, with a lower energy than the metallic state. Two similar compounds CsTlCl_3 and CsTlF_3 have been synthesized and found to be insulators.³⁸ Labeling the In ion with more charge on it (which we identify as corresponding to the formal 1+ oxidation state) to be In1 and the In ion with less charge on it (which we identify as corresponding to the formal 3+ oxidation state) to be In2, then the valence band of $\text{Rb}_2\text{InInBr}_6$

is derived from antibonding states between In1-s and Br-p orbitals and conduction band derived from antibonding states between In2-s and Cl-p orbitals. This interpretation is better supported by the crystal orbital Hamilton population analysis in the Supporting Information Figure S6. Both the valence band and conduction band are very dispersive due to their *s* character, resulting in very small electron and hole effective masses.

Optical Absorption and Spectroscopic Limited Maximum Efficiency. Absorption properties relevant to photovoltaic applications depend not only on the band gap but also on the nature of the gap, i.e., direct or indirect, dipole allowed, or forbidden. The absorption spectra for compounds from the five categories are presented in Figures S7–S12. The onsets of all compounds are close to their dipole-allowed band gaps E_g^{da} (matrix element squared $|\mathcal{M}|^2 > 10^{-6} \text{ eV}^2/\text{\AA}^2$). For category 1 and category 2 compounds, E_g^{da} is the fundamental band gap. For the other three categories with indirect band gaps, E_g^{da} is significantly larger than the fundamental band gap E_g , as shown in Figure 4, where the dots indicate E_g and arrows indicate E_g^{da} . So, it is reasonable that we use direct band gap instead of fundamental band gap in the first screening steps.

Based on absorption spectra, we then calculate the spectroscopic limited maximum efficiency (SLME) as defined by Yu and Zunger.⁴³ SLME takes consideration of the band gap, the shape of absorption spectra, and nonradiative recombination losses. The fraction of radiative recombination current is an exponentially decaying function with the decay rate determined by $E_g^{\text{da}} - E_g$. A larger $E_g^{\text{da}} - E_g$ indicates more severe nonradiative recombination losses. SLMEs for all 30 compounds are plotted versus their band gaps in Figure 4. Category 2 compounds form a curve very similar to that of the Shockley–Queisser limit. This is not surprising since the assumptions made when calculating the Shockley–Queisser limit are good approximations for category 2 compounds, where the radiative recombination dominates and the

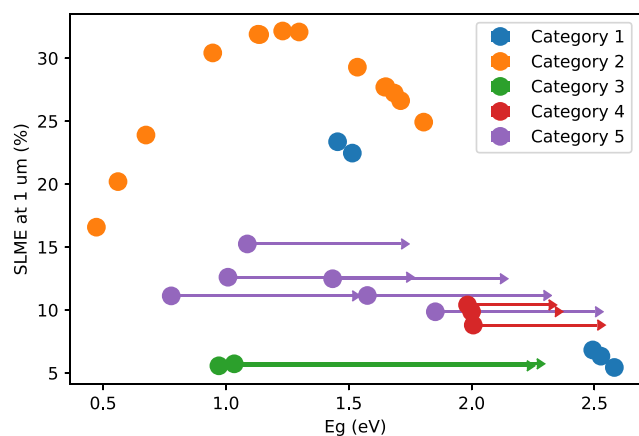


Figure 4. SLME at $L = 1 \mu\text{m}$ vs the fundamental gap E_g for compounds from the 5 categories. For categories 3, 4, and 5, the arrow indicates the direct dipole-allowed band gap E_g^{da} .

absorption onsets are sharp. For category 1 compounds, even though they are direct gap semiconductors, their absorption onset is not as sharp as category 2 compounds, as it takes over 0.5 eV for their absorption coefficients to rise up to 10^4 cm^{-1} (Figure S7). As discussed by Meng et al., category 1 compounds exhibit parity-forbidden transitions only between CBM and VBM but with allowed transitions between band edges at other k -points.²⁴ As a result, the SLMEs for category 1 compounds are lower than category 2 compounds at similar band gaps. Category 3 compounds have lowest efficiencies among the five categories, due to their large direct band gaps as well as large nonradiative recombination losses caused by a large $E_g^{\text{da}} - E_g$. Category 4 compounds have higher efficiencies than category 3 compounds with similar direct band gaps, probably due to the smaller difference between E_g^{da} and E_g in category 4 compounds. Category 5 compounds have the best efficiency among the indirect gap compounds, because some of category 5 compounds have band gaps closer to the ideal value. Overall, the direct gap compounds (category 1 and 2) achieve better SLMEs than the indirect gap compounds, with the best featuring theoretically predicted efficiency higher than 30%.

Dynamical Stability Analysis. As mentioned above, it is possible that, particularly at low temperature, some of the double perovskite compounds in the high-symmetry $Fm\bar{3}m$ structure may be dynamically unstable with respect to

symmetry-lowering phonon modes associated with ferroelectric, octahedral-rotation, and related structural distortions. To investigate this issue, for all 30 compounds identified above, dynamical stability is evaluated by calculating phonon spectra at 0 K. The least-stable phonon frequencies (i.e., the lowest real frequency for dynamically stable compounds and the imaginary frequency with the largest magnitude for dynamically unstable compounds) and related q -points are listed in Table S6. Also listed in Table S6 is the space group of the distorted structure that results from the introduction of the least-stable phonon mode; for the correspondence between this space group and the distortion mode, the interested is referred to ref 37. Two of the compounds ($\text{Cs}_2\text{AgInCl}_6$ and $\text{Cs}_2\text{InAsBr}_6$) have no imaginary modes and are dynamically stable at 0 K. All other compounds have imaginary modes at 0 K, mostly at Γ . For five of the compounds, the frequencies of the imaginary modes are larger than 10 THz, and we consider them to be dynamically unstable. For all other 23 compounds with smaller imaginary frequencies, it is still possible that the phonon entropy at finite temperatures can stabilize these modes at room temperature. For these compounds, we imposed structural distortions corresponding to the most unstable phonon mode at Γ and performed structural relaxations; the energy differences between the resulting relaxed distorted structures and the ideal cubic structure are listed in Table S6. If this structural energy difference is smaller than 10 meV/atom, we consider the compounds as candidates for stability in the cubic phase at room temperature. Out of the 25 compounds with small or no imaginary frequencies, 14 meet this criterion: 3 from category 1, 7 from category 2, 1 from category 3, and 3 from category 5.

Combining with SLMEs calculated above, in Table 2, we summarize the 11 compounds that have SLMEs larger than 10%, are thermodynamically stable, and either dynamically stable or possibly dynamically stable at room temperature (based on the energetic criterion above). The $d^{10}s^2$ configuration of the band edges for category 2 compounds resembles that of hybrid lead halides, so it is not surprising that most of the promising compounds come from category 2. Of these compounds, those containing In may be more attractive than those containing Tl, due to the toxicity of the latter element.

Chemical Trend Analysis. The efficiencies or stability of a compound can be improved further by substitutional alloying,

Table 2. $\text{MM}'\text{X}_6$ Compounds (11) that Are Both Thermodynamically and Dynamically Stable and have SLMEs Larger than 10%^a

formula	category	SLME at $1 \mu\text{m}$ (%)	m_e	m_h	E_{hull}	$E_{\text{cubic}} - E_{\text{distorted}}$
$\text{Cs}_2\text{AgInBr}_6$	1	22.5	0.18	0.71	0.0	0.0
$\text{Cs}_2\text{InAsBr}_6$	2	20.2	0.30	0.05	26.2	0.0
$\text{Cs}_2\text{InBiCl}_6$	2	24.9	0.39	0.18	14.2	8.2
$\text{Cs}_2\text{InBiBr}_6$	2	31.9	0.32	0.11	0.0	6.8
$\text{Cs}_2\text{InSbBr}_6$	2	23.9	0.31	0.07	7.0	2.6
$\text{Cs}_2\text{TlAsBr}_6$	2	27.7	0.31	0.15	0.0	1.6
$\text{Cs}_2\text{TlAsI}_6$	2	32.1	0.23	0.13	0.0	3.1
$\text{Cs}_2\text{TlSbBr}_6$	2	27.7	0.31	0.16	12.4	9.0
$\text{Cs}_2\text{InGaI}_6$	5	11.1	0.22	0.51	18.1	1.1
$\text{Cs}_2\text{InInBr}_6$	5	11.2	0.27	0.58	0.0	2.3
$\text{Cs}_2\text{TlTlBr}_6$	5	15.2	0.26	0.58	0.7	6.8

^aChemical formula, category, calculated SLME at $L = 1 \mu\text{m}$, effective masses, energies above hull (meV/atom), and $E_{\text{cubic}} - E_{\text{distorted}}$ (meV/atom) are listed below.

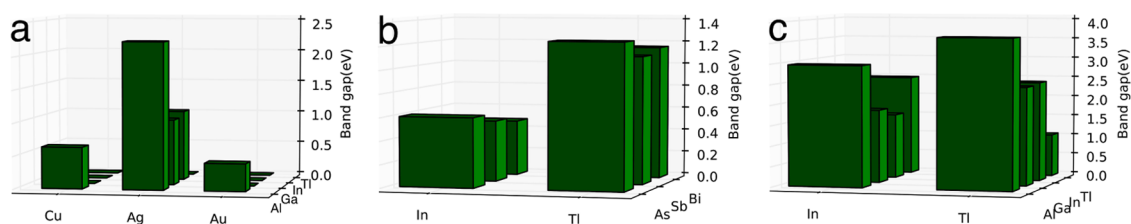


Figure 5. Chemical trends of band gaps calculated by PBE + SOC for $\text{Cs}_2\text{MM}'\text{Cl}_6$ with (a) $M = \text{Cu, Ag, Au}$ and $M' = \text{Al, Ga, In, Tl}$ (category 1), (b) $M = \text{In, Tl}$ and $M' = \text{As, Sb, Bi}$ (category 2), and (c) $M = \text{In, Tl}$ and $M' = \text{Al, Ga, In, Tl}$ (category 5).

especially with elements from the same group. A detailed analysis of chemical trends with respect to band structures within the three promising chemical categories defined above may be useful in guiding such band structure engineering. To analyze the chemical trends of band gaps for the promising categories 1, 2 and 5, band gaps are calculated for compounds within each category with the GGA-PBE functional including SOC effects. Band gaps for $\text{Cs}_2\text{MM}'\text{Cl}_6$ compounds with $M = \text{Cu, Ag, Au, In, Tl}$ and $M' = \text{Al, Ga, In, Tl, As, Sb, Bi}$ are plotted in Figure 5.

For $\text{Cs}_2\text{MM}'\text{Cl}_6$ compounds, with $M = \text{Cu, Ag, Au}$ and $M' = \text{Al, Ga, In, Tl}$ (Figure 5a, category 1), Ag-containing compounds have larger band gaps than those with Cu and Au. This can be understood considering that among Cu, Ag, and Au, Ag has the lowest-energy d states and the valence band maximum (VBM) derives from hybridization between Cu/Ag/Au-d and Cl-p orbitals, such that the lowest VBM for Ag compounds results in the largest band gap. For the $M = \text{Ag}$ series, for $M' = \text{Ga, In, Tl}$, the CBM is derived from antibonding M' -s and Cl-p states. The band gap of $\text{Cs}_2\text{AgTlCl}_6$ is the smallest, due to the relativistic stabilization of Tl-s states and small bonding–antibonding splitting caused by relatively small energetic overlap and spatial overlap of the Tl–Cl bond. For $\text{Cs}_2\text{AgAlCl}_6$, the Al-s state is shallow, and the hybridization of Al–Cl is strong, leading to a high lying Al–Cl antibonding level. In this case, the CBM is no longer Al–Cl states but Ag–Cl states. The band gap of $\text{Cs}_2\text{AgAlCl}_6$ is the largest among the $M = \text{Ag}$ series.

For $\text{Cs}_2\text{MM}'\text{Cl}_6$ compounds, with $M = \text{In, Tl}$ and $M' = \text{As, Sb, Bi}$ (Figure 5b, category 2), Tl compounds have larger band gaps than In compounds. Due to relativistic effects, Tl-s is lower in energy than In-s, resulting in a lower VBM. For the $M = \text{In}$ series, the band gap difference among As, Sb, Bi is very small, probably because the band edges all have contributions from In-s and In-p states and the band gaps are affected less by the difference among As, Sb, and Bi. For the $M = \text{Tl}$ series, the band gap difference among As, Sb, Bi is also very small, likely due to the same underlying reason.

For $\text{Cs}_2\text{MM}'\text{Cl}_6$ compounds, with $M = \text{In, Tl}$ and $M' = \text{Al, Ga, In, Tl}$ (Figure 5c, category 5), for the $M = \text{Tl}$ series, the CBM is derived from antibonding M' -s and Cl-p characters (Tl: 1+, M' : 3+). The band gap of $\text{Cs}_2\text{TlAlCl}_6$ is the largest, due to the shallow Al-s orbital and large bonding–antibonding splitting caused by the relatively large spatial overlap and energetic overlap of the Al–Cl bond. The band gap of $\text{Cs}_2\text{TlTlCl}_6$ is the smallest in the series, since the CBM and VBM are derived from the same Tl-s character. For the $M = \text{In}$ series, for $M' = \text{Tl, In, Ga}$, the VBM is derived from antibonding M' -s and Cl-p characters (M' : 1+, In: 3+). The band gap of $\text{Cs}_2\text{TlInCl}_6$ is the largest, due to the relativistic stabilization of Tl-s orbitals and the small bonding–antibonding splitting caused by relatively small energetic

overlap and spatial overlap of the Tl–Cl bond. The band gap of $\text{Cs}_2\text{InInCl}_6$ is the smallest in the series, since the CBM and VBM are derived from the same In-s character.

SUMMARY AND DISCUSSION

Starting from a consideration of the octahedral and tolerance factors of 1980 candidate double perovskite compounds, we compute structural, thermodynamic, and electronic properties of 1149 compounds using first-principles calculations. The computational results have been assembled in a database that is accessible through the Materials Project online.

We present the application of the database in screening for new double perovskite halide compounds showing promising electronic properties for photovoltaic solar absorber applications. Combining further calculations of optical absorption, conversion efficiency, and phonon stability, 11 promising candidates (summarized in Table 2) from 3 categories were identified from the database. Among them, 7 of these compounds are from a chemical class corresponding to M/M' electronic configurations of $d^{10}s^2/d^{10}s^2$, isoelectronic to the hybrid lead halides. All 11 compounds have not been reported experimentally, and they are listed below with the SLME value at 1 μm in the parentheses: $\text{Cs}_2\text{AgInBr}_6$ (22.5%), $\text{Cs}_2\text{InAsBr}_6$ (20.2%), $\text{Cs}_2\text{InBiCl}_6$ (24.9%), $\text{Cs}_2\text{InBiBr}_6$ (31.9%), $\text{Cs}_2\text{InSbBr}_6$ (23.9%), $\text{Cs}_2\text{TlAsBr}_6$ (27.7%), $\text{Cs}_2\text{TlAsI}_6$ (32.1%), $\text{Cs}_2\text{TlSbBr}_6$ (27.7%), $\text{Cs}_2\text{InGaI}_6$ (11.1%), $\text{Cs}_2\text{InInBr}_6$ (11.2%), $\text{Cs}_2\text{TlTlBr}_6$ (15.2%).

The chemical trends for the band gap within each of three different chemical categories are identified as follows: (1) category 1: for $\text{Cs}_2\text{MM}'\text{Cl}_6$ compounds, with $M = \text{Cu, Ag, Au}$ and $M' = \text{Al, Ga, In, Tl}$, silver compounds always have larger band gaps than those with Cu and Au with the same M' elements; the band gap trend for M' site is $\text{Al} > \text{In, Ga} > \text{Tl}$. (2) category 2: for $\text{Cs}_2\text{MM}'\text{Cl}_6$ compounds, with $M = \text{In, Tl}$ and $M' = \text{As, Sb, Bi}$, thallium compounds are found to have larger band gaps than In compounds, confirming results of a previous study.²³ (3) Category 5: for $\text{Cs}_2\text{MM}'\text{Cl}_6$ compounds, with $M = \text{Tl}$ and $M' = \text{Al, Ga, In, Tl}$, the band gap trend for M' site is $\text{Al} > \text{In, Ga} > \text{Tl}$. For $\text{Cs}_2\text{MM}'\text{Cl}_6$ compounds, with $M = \text{In}$ and $M' = \text{Ga, In, Tl}$, the band gap trend for M' site is $\text{Tl} > \text{Ga, In}$. These trends can provide guidelines for the use of substitutional alloying as a means of tuning band structures in halide perovskite solid solutions.

In addition to the potential solar-cell applications discussed specifically above, the halide double perovskite database developed in this work can be used for other applications, such as scintillators. For scintillator applications, it is usually required that the host materials have large enough band gap to accommodate dopant-ion energy levels involved in relevant electronic transitions. An overview of our database shows that the compounds with alkali metals as M site cations usually have significantly larger band gaps than compounds with other

M site elements. Such compounds potentially can be engineered toward scintillator applications, and indeed the compounds $\text{Cs}_2\text{LiYCl}_6$ and $\text{Cs}_2\text{NaYBr}_3\text{I}_3$ have already been identified as relevant examples.^{4,55} The calculations for this database yielded a mixed-valence charge-ordered state for ATiX_3 , consistent with experimental results,³⁸ and also predicted a mixed-valence state for AlInX_3 compounds. It is possible that some of these structures or their alloys could be precursors for superconducting compounds, as discussed in ref 38. Overall, it is anticipated that the database of halide double perovskite compounds developed in this work and made available online could find application in materials discovery efforts for a wider variety of applications than those considered here.

■ ASSOCIATED CONTENT

Supporting Information

The Supporting Information is available free of charge on the ACS Publications website at DOI: 10.1021/acs.chemmater.9b00116.

PBE band gaps for all considered compounds, –COHP calculations of $\text{Cs}_2\text{MM}'\text{Cl}_6$ compounds, structural information for experimentally reported halide double perovskite compounds, and calculated lattice parameters, band gaps, energy above hull, effective masses, SLMs, absorption spectra, and phonon frequencies for the candidate compounds (PDF)

■ AUTHOR INFORMATION

Corresponding Authors

*E-mail: yaocai@berkeley.edu (Y.C.).

*E-mail: mdasta@berkeley.edu (M.A.).

ORCID

Yao Cai: 0000-0002-0815-7366

P. C. Harikesh: 0000-0002-2488-1821

Biplab Ghosh: 0000-0002-5584-1830

Kristin A. Persson: 0000-0003-2495-5509

Nripan Mathews: 0000-0001-5234-0822

Subodh G. Mhaisalkar: 0000-0002-9895-2426

Matthew Sherburne: 0000-0002-3992-1822

Notes

The authors declare no competing financial interest.

■ ACKNOWLEDGMENTS

This work was funded primarily by the National Research Foundation (NRF), Singapore (CRP NRF2014NRF-CRP002-036 and NRF-CRP14-2014-03), and the Singapore-Berkeley Research Initiative for Sustainable Energy (SinBeRISE) CREATE programme. The use was made of computational resources provided under the Extreme Science and Engineering Discovery Environment (XSEDE), which is supported by the National Science Foundation grant no. OCI-1053575. The efforts of P.H., K.A.P., and M.A., associated with the integration of the database into Materials Project (P.H. and K.A.P.) and supervising the computational work and its analysis (M.A.), were funded by the U.S. Department of Energy, Office of Science, Office of Basic Energy Sciences, Materials Sciences and Engineering Division under Contract No. DE-AC02-05-CH11231 (Materials Project program KC23MP).

■ REFERENCES

- (1) Greul, E.; Petrus, M. L.; Binek, A.; Docampo, P.; Bein, T. Highly Stable, Phase Pure $\text{Cs}_2\text{AgBiBr}_6$ Double Perovskite Thin Films for Optoelectronic Applications. *J. Mater. Chem. A* **2017**, *5*, 19972–19981.
- (2) Luo, J.; Li, S.; Wu, H.; Zhou, Y.; Li, Y.; Liu, J.; Li, J.; Li, K.; Yi, F.; Niu, G.; Tang, J. $\text{Cs}_2\text{AgInCl}_6$ Double Perovskite Single Crystals: Parity Forbidden Transitions and Their Application For Sensitive and Fast UV Photodetectors. *ACS Photonics* **2018**, *5*, 398–405.
- (3) Pan, W.; et al. $\text{Cs}_2\text{AgBiBr}_6$ Single-crystal X-ray Detectors with a Low Detection Limit. *Nat. Photonics* **2017**, *11*, 726–732.
- (4) Glodo, J.; Hawrami, R.; Shah, K. S. Development of $\text{Cs}_2\text{LiYCl}_6$ Scintillator. *J. Cryst. Growth* **2013**, *379*, 73–78.
- (5) Jain, A.; Ong, S. P.; Hautier, G.; Chen, W.; Richards, W. D.; Dacek, S.; Cholia, S.; Gunter, D.; Skinner, D.; Ceder, G.; Persson, K. The Materials Project: A Materials Genome Approach to Accelerating Materials Innovation. *APL Mater.* **2013**, *1*, 011002–011012.
- (6) Chakraborty, S.; Xie, W.; Mathews, N.; Sherburne, M.; Ahuja, R.; Asta, M.; Mhaisalkar, S. G. Rational Design: A High-Throughput Computational Screening and Experimental Validation Methodology for Lead-Free and Emergent Hybrid Perovskites. *ACS Energy Lett.* **2017**, *2*, 837–845.
- (7) Slavney, A. H.; Hu, T.; Lindenberg, A. M.; Karunadasa, H. I. A Bismuth-Halide Double Perovskite with Long Carrier Recombination Lifetime for Photovoltaic Applications. *J. Am. Chem. Soc.* **2016**, *138*, 2138–2141.
- (8) Ning, W.; Wang, F.; Wu, B.; Lu, J.; Yan, Z.; Liu, X.; Tao, Y.; Liu, J.-M.; Huang, W.; Fahlman, M.; Hultman, L.; Sum, T. C.; Gao, F. Long Electron-Hole Diffusion Length in High-Quality Lead-Free Double Perovskite Films. *Adv. Mater.* **2018**, *30*, No. 1706246.
- (9) Wei, F.; Deng, Z.; Sun, S.; Zhang, F.; Evans, D. M.; Kieslich, G.; Tominaka, S.; Carpenter, M. A.; Zhang, J.; Bristowe, P. D.; Cheetham, A. K. Synthesis and Properties of a Lead-Free Hybrid Double Perovskite: $(\text{CH}_3\text{NH}_3)_2\text{AgBiBr}_6$. *Chem. Mater.* **2017**, *29*, 1089–1094.
- (10) Volonakis, G.; Filip, M. R.; Haghighirad, A. A.; Sakai, N.; Wenger, B.; Snaith, H. J.; Giustino, F. Lead-Free Halide Double Perovskites via Heterovalent Substitution of Noble Metals. *J. Phys. Chem. Lett.* **2016**, *7*, 1254–1259.
- (11) McClure, E. T.; Ball, M. R.; Windl, W.; Woodward, P. M. $\text{Cs}_2\text{AgBiX}_6$ (X = Br, Cl): New Visible Light Absorbing, Lead-Free Halide Perovskite Semiconductors. *Chem. Mater.* **2016**, *28*, 1348–1354.
- (12) Creutz, S. E.; Crites, E. N.; De Siena, M. C.; Gamelin, D. R. Colloidal Nanocrystals of Lead-Free Double-Perovskite (Elpasolite) Semiconductors: Synthesis and Anion Exchange To Access New Materials. *Nano Lett.* **2018**, *18*, 1118–1123.
- (13) Tran, T. T.; Panella, J. R.; Chamorro, J. R.; Morey, J. R.; McQueen, T. M. Designing Indirect-direct Bandgap Transitions in Double Perovskites. *Mater. Horizons* **2017**, *4*, 688–693.
- (14) Wei, F.; Deng, Z.; Sun, S.; Xie, F.; Kieslich, G.; Evans, D. M.; Carpenter, M. A.; Bristowe, P. D.; Cheetham, A. K. The Synthesis, Structure and Electronic Properties of a Lead-free Hybrid Inorganic-organic Double Perovskite $(\text{MA})_2\text{KBiCl}_6$ (MA = Methylammonium). *Mater. Horizons* **2016**, *3*, 328–332.
- (15) Savory, C. N.; Walsh, A.; Scanlon, D. O. Can Pb-Free Halide Double Perovskites Support High-Efficiency Solar Cells? *ACS Energy Lett.* **2016**, *1*, 949–955.
- (16) Deng, Z.; Wei, F.; Sun, S.; Kieslich, G.; K. Cheetham, A.; D. Bristowe, P. Exploring the Properties of Lead-free Hybrid Double Perovskites Using a Combined Computational-experimental Approach. *J. Mater. Chem. A* **2016**, *4*, 12025–12029.
- (17) Volonakis, G.; Haghighirad, A. A.; Milot, R. L.; Sio, W. H.; Filip, M. R.; Wenger, B.; Johnston, M. B.; Herz, L. M.; Snaith, H. J.; Giustino, F. $\text{Cs}_2\text{InAgCl}_6$: A New Lead-Free Halide Double Perovskite with Direct Band Gap. *J. Phys. Chem. Lett.* **2017**, *8*, 772–778.
- (18) Zhou, J.; Xia, Z.; S. Molokeev, M.; Zhang, X.; Peng, D.; Liu, Q. Composition Design, Optical Gap and Stability Investigations of Lead-free Halide Double Perovskite $\text{Cs}_2\text{AgInCl}_6$. *J. Mater. Chem. A* **2017**, *5*, 15031–15037.

- (19) Slavney, A. H.; Leppert, L.; Bartesaghi, D.; Gold-Parker, A.; Toney, M. F.; Savenije, T. J.; Neaton, J. B.; Karunadasa, H. I. Defect-Induced Band-Edge Reconstruction of a Bismuth-Halide Double Perovskite for Visible-Light Absorption. *J. Am. Chem. Soc.* **2017**, *139*, 5015–5018.
- (20) Du, K.-z.; Meng, W.; Wang, X.; Yan, Y.; Mitzi, D. B. Bandgap Engineering of Lead-Free Double Perovskite $\text{Cs}_2\text{AgBiBr}_6$ through Trivalent Metal Alloying. *Angew. Chem., Int. Ed.* **2017**, *56*, 8158–8162.
- (21) Filip, M. R.; Liu, X.; Miglio, A.; Hautier, G.; Giustino, F. Phase Diagrams and Stability of Lead-Free Halide Double Perovskites $\text{Cs}_2\text{BB}'\text{X}_6$; B = Sb and Bi, B' = Cu, Ag, and Au, and X = Cl, Br, and I. *J. Phys. Chem. C* **2018**, *122*, 158–170.
- (22) Volonakis, G.; Haghghirad, A. A.; Snaith, H. J.; Giustino, F. Route to Stable Lead-Free Double Perovskites with the Electronic Structure of $\text{CH}_3\text{NH}_3\text{PbI}_3$: A Case for Mixed-Cation $[\text{Cs}(\text{CH}_3\text{NH}_3)_2\text{CH}(\text{NH}_2)_2]\text{InBiBr}_6$. *J. Phys. Chem. Lett.* **2017**, *8*, 3917–3924.
- (23) Zhao, X.-G.; Yang, J.-H.; Fu, Y.; Yang, D.; Xu, Q.; Yu, L.; Wei, S.-H.; Zhang, L. Design of Lead-Free Inorganic Halide Perovskites for Solar Cells via Cation-Transmutation. *J. Am. Chem. Soc.* **2017**, *139*, 2630–2638.
- (24) Meng, W.; Wang, X.; Xiao, Z.; Wang, J.; Mitzi, D. B.; Yan, Y. Parity-Forbidden Transitions and Their Impact on the Optical Absorption Properties of Lead-Free Metal Halide Perovskites and Double Perovskites. *J. Phys. Chem. Lett.* **2017**, *8*, 2999–3007.
- (25) Zhao, X.-G.; Yang, D.; Sun, Y.; Li, T.; Zhang, L.; Yu, L.; Zunger, A. Cu-In Halide Perovskite Solar Absorbers. *J. Am. Chem. Soc.* **2017**, *139*, 6718–6725.
- (26) Dai, J.; Ma, L.; Ju, M.; Huang, J.; ChengZeng, X. In- and Gd-based Inorganic Double Perovskites with Direct Bandgaps for Photovoltaic Applications. *Phys. Chem. Chem. Phys.* **2017**, *19*, 21691–21695.
- (27) Jain, A.; Voznyy, O.; Sargent, E. H. High-Throughput Screening of Lead-Free Perovskite-like Materials for Optoelectronic Applications. *J. Phys. Chem. C* **2017**, *121*, 7183–7187.
- (28) Kojima, N.; Hasegawa, M.; Kitagawa, H.; Kikigawa, T.; Shimomura, O. P-T Phase Diagram and Gold Valence State of the Perovskite-Type Mixed-Valence Compounds $\text{Cs}_2\text{Au}_2\text{X}_6$ (X = Cl, Br, and I) under High Pressures. *J. Am. Chem. Soc.* **1994**, *116*, 11368–11374.
- (29) Matsushita, N.; Kitagawa, H.; Kojima, N. A. Three-Dimensional Iodo-Bridged Mixed-Valence Gold(I, III) Compound, $\text{Cs}_2\text{Au}^{\text{I}}\text{Au}^{\text{III}}\text{I}_6$. *Acta Crystallogr., Sect. C: Cryst. Struct. Commun.* **1997**, *53*, 663–666.
- (30) Liu, X. J.; Matsuda, K.; Moritomo, Y.; Nakamura, A.; Kojima, N. Electronic Structure of the Gold Complexes $\text{Cs}_2\text{Au}_2\text{X}_6$ (X = I, Br, and Cl). *Phys. Rev. B* **1999**, *59*, 7925–7930.
- (31) Wang, S.; Kemper, A. F.; Baldini, M.; Shapiro, M. C.; Riggs, S. C.; Zhao, Z.; Liu, Z.; Devereaux, T. P.; Geballe, T. H.; Fisher, I. R.; Mao, W. L. Bandgap Closure and Reopening in CsAuI_3 at High Pressure. *Phys. Rev. B* **2014**, *89*, No. 245109.
- (32) Debbichi, L.; Lee, S.; Cho, H.; Rappe, A. M.; Hong, K.-H.; Jang, M. S.; Kim, H. Mixed Valence Perovskite $\text{Cs}_2\text{Au}_2\text{I}_6$: A Potential Material for Thin-Film Pb-Free Photovoltaic Cells with Ultrahigh Efficiency. *Adv. Mater.* **2018**, *30*, No. 1707001.
- (33) Blöchl, P. E. Projector Augmented-wave Method. *Phys. Rev. B* **1994**, *50*, 17953–17979.
- (34) Kresse, G.; Furthmüller, J. Efficient Iterative Schemes for *ab initio* Total-energy Calculations Using a Plane-wave Basis Set. *Phys. Rev. B* **1996**, *54*, 11169–11186.
- (35) Kresse, G.; Furthmüller, J. Efficiency of *Ab-initio* Total Energy Calculations for Metals and Semiconductors Using a Plane-wave Basis Set. *Comput. Mater. Sci.* **1996**, *6*, 15–50.
- (36) Kresse, G.; Hafner, J. *Ab initio* Molecular Dynamics for Liquid Metals. *Phys. Rev. B* **1993**, *47*, 558–561.
- (37) Howard, C. J.; Kennedy, B. J.; Woodward, P. M. Ordered Double Perovskites - a Group-theoretical analysis. *Acta Crystallogr., Sect. B: Struct. Sci.* **2003**, *59*, 463–471.
- (38) Retuerto, M.; et al. Synthesis and Properties of Charge-Ordered Thallium Halide Perovskites, $\text{CsTl}_{0.5}\text{Tl}_{0.5}^3\text{X}_3$ (X = F or Cl): Theoretical Precursors for Superconductivity? *Chem. Mater.* **2013**, *25*, 4071–4079.
- (39) Blöchl, P. E.; Jepsen, O.; Andersen, O. K. Improved Tetrahedron Method for Brillouin-zone Integrations. *Phys. Rev. B* **1994**, *49*, 16223–16233.
- (40) Hautier, G.; Miglio, A.; Ceder, G.; Rignanese, G.-M.; Gonze, X. Identification and Design Principles of Low Hole Effective Mass p-type Transparent Conducting Oxides. *Nat. Commun.* **2013**, *4*, No. 2292.
- (41) Madsen, G. K. H.; Singh, D. J. BoltzTraP. A Code for Calculating Band-structure Dependent Quantities. *Comput. Phys. Commun.* **2006**, *175*, 67–71.
- (42) Ong, S. P.; Richards, W. D.; Jain, A.; Hautier, G.; Kocher, M.; Cholia, S.; Gunter, D.; Chevrier, V. L.; Persson, K. A.; Ceder, G. Python Materials Genomics (pymatgen): A Robust, Open-source Python Library for Materials Analysis. *Comput. Mater. Sci.* **2013**, *68*, 314–319.
- (43) Yu, L.; Zunger, A. Identification of Potential Photovoltaic Absorbers Based on First-Principles Spectroscopic Screening of Materials. *Phys. Rev. Lett.* **2012**, *108*, No. 068701.
- (44) Togo, A.; Tanaka, I. First Principles Phonon Calculations in Materials Science. *Scr. Mater.* **2015**, *108*, 1–5.
- (45) Shannon, R. D. Revised Effective Ionic Radii and Systematic Studies of Interatomic Distances in Halides and Chalcogenides. *Acta Crystallogr., Sect. A* **1976**, *32*, 751–767.
- (46) Li, W.; Ionescu, E.; Riedel, R.; Gurlo, A. Can We Predict the Formability of Perovskite Oxynitrides from Tolerance and Octahedral Factors? *J. Mater. Chem. A* **2013**, *1*, 12239–12245.
- (47) Goldschmidt, V. M. Die Gesetze der Krystallochemie. *Naturwissenschaften* **1926**, *14*, 477–485.
- (48) Belsky, A.; Hellenbrandt, M.; Karen, V. L.; Luksch, P. New Developments in the Inorganic Crystal Structure Database (ICSD): Accessibility in Support of Materials Research and Design. *Acta Crystallogr., Sect. B: Struct. Sci.* **2002**, *58*, 364–369.
- (49) Bergerhoff, G.; Hundt, R.; Sievers, R.; Brown, I. D. The Inorganic Crystal Structure Data Base. *J. Chem. Inf. Model.* **1983**, *23*, 66–69.
- (50) Travis, W.; Glover, E. N. K.; Bronstein, H.; Scanlon, D. O.; Palgrave, R. G. On the Application of the Tolerance Factor to Inorganic and Hybrid Halide Perovskites: a Revised System. *Chem. Sci.* **2016**, *7*, 4548–4556.
- (51) Sun, W.; Dacek, S. T.; Ong, S. P.; Hautier, G.; Jain, A.; Richards, W. D.; Gamst, A. C.; Persson, K. A.; Ceder, G. The Thermodynamic Scale of Inorganic Crystalline Metastability. *Sci. Adv.* **2016**, *2*, No. e1600225.
- (52) Krishnamoorthy, T.; Ding, H.; Yan, C.; Leong, W. L.; Baikie, T.; Zhang, Z.; Sherburne, M.; Li, S.; Asta, M.; Mathews, N.; Mhaisalkar, S. G. Lead-free Germanium Iodide Perovskite Materials for Photovoltaic Applications. *J. Mater. Chem. A* **2015**, *3*, 23829–23832.
- (53) Cai, Y.; Xie, W.; Ding, H.; Chen, Y.; Thirumal, K.; Wong, L. H.; Mathews, N.; Mhaisalkar, S. G.; Sherburne, M.; Asta, M. Computational Study of Halide Perovskite-Derived A_2BX_6 Inorganic Compounds: Chemical Trends in Electronic Structure and Structural Stability. *Chem. Mater.* **2017**, *29*, 7740–7749.
- (54) Yu, P. Y.; Cardona, M. *Fundamentals of Semiconductors*, 4th ed.; Springer-Verlag: Berlin Heidelberg, 2010.
- (55) Wei, H.; Du, M.-H.; Stand, L.; Zhao, Z.; Shi, H.; Zhuravleva, M.; Melcher, C. L. Scintillation Properties and Electronic Structures of the Intrinsic and Extrinsic Mixed Elpasolites $\text{Cs}_2\text{NaRBr}_3\text{I}_3$ (R = La, Y). *Phys. Rev. Appl.* **2016**, *5*, No. 024008.